

Design and Development of Advanced MoSe₂/MnO₂ Nanocomposite for Direct yellow dye degradation for Enhanced photocatalytic Applications

Gokulnath Dhanasekaran ^a, Nisha Parthiban ^a, Nithya. N ^b, D. Karthigaimuthu ^a,
G. Vijayakumar ^b, Sangaraju Sambasivam ^c, T. Elangovan^{a, *}

^a Smart Energy Materials Research Laboratory (SEMRL), Department of Energy Science and Technology, Periyar University, Salem, India-636011

^b Department of Physics, PSG College of arts and Science, Coimbatore, India

^c National Water and Energy Center, United Arab Emirates University, Al Ain, 15551, UAE

Abstract

MoSe₂, a significant component within the class of two-dimensional transition metal dichalcogenides, boasts a diverse set of photoelectrochemical characteristics. Herein, we propose a simple hydrothermal approach to synthesis MoSe₂/MnO₂ nanocomposites with controllable morphologies with enhanced photocatalytic activity. The obtained nanocomposite was confirmed by the analysed peaks of MoSe₂/MnO₂ observed in X-ray diffraction (13.6°, 18.1°, 37.5°), infrared spectra (495, 645, 1410 cm⁻¹), UV-Vis spectra (506, 640, 748 nm) and the band gap lowering (1.94 eV, 2.8 eV, and 4.57 eV). Due to the efficient separation of photogenerated electron-hole pairs facilitated by the rapid transfer of photogenerated electrons by the addition of MnO₂, the MoSe₂/MnO₂ composite demonstrates significantly enhanced solar-driven photocatalytic performance and excellent stability in degrading Direct Yellow (DY), a common pollutant found in industrial effluents. The MoSe₂/MnO₂ nanocomposite photocatalytic activity was found to be 1.2 to 1.6 times higher than that of its individual components of MoSe₂ and MnO₂, indicating synergistic effects leading to enhanced performance. This underscores its considerable potential for environmental remediation, offering a promising approach for the degradation of harmful industrial chemicals present in wastewater using sunlight.

Keywords: Molybdenum diselenide; Manganese dioxide; Nanocomposite; Photocatalysis; UV-Vis light

1. Introduction

The absorption of the semiconductor photocatalysts could be reducing the energy shortages while also removing pollutants from the environment [1], [2], [3]. For water pollutant treatment, it is very important to effectively convert solar light to active species. UV-Vis light photocatalysts are of great interests due to their extremely solar light utilizations. In recent years, transition metal dichalcogenides (TMDs) [4], [5], semiconductor – based photocatalysts viz, TiO₂ [6], ZnO [7], BiVO₄ [8], etc. have been studied as UV-Vis light photocatalytic material also among these materials, MoSe₂ is a promising candidate because it has a narrow bandgap for harvesting extremely sunlight [9]. It also possesses unique two- dimensional (2D) layered structure for surface reactions and it has good absorbance stability [10], [11]. However, the ease of charge recombination strongly decreases photocatalytic activity and limit its applications in water pollutant treatment. To satisfy these properties of MoSe₂ is an efficient strategy to separate the photo-generated charge carriers and reduce its internal recombination [12], [13], [14]. As a well-known oxide semiconductor, MnO₂ could generate superoxide radical and hydroxyl radical, respectively. These oxidizing radicals could effectively decompose various organic compounds [15], [16], [17], [18]. Among the different combination of forming MoSe₂/MnO₂ nanocomposite, it could be a good photocatalyst for pollutant treatment. However, it is still a challenge to controllable construct MoSe₂/MnO₂ nanocomposite with uniform interface and good dispersion.

So far combination of MoSe₂/MnO₂ nanocomposite were usually prepared by a different nano structure growth process. For example, some researchers analysed MoSe₂ nanosheets on MnO₂ nanorods [19], [20], [21], while the others grew oxides on MoSe₂ [22]. In comparison with these nanostructures which are easily agglomerate, the interface contact and uniformly could be more controllable when MnO₂ nanostructure were used as growing supports. And tuning network porosity and large amounts of active sites [23], [24], [25], [26]. These advantages are favourable for mass transport, surface nucleation and growth process, furthermore, their ultralong zero-dimensional structure might be also favour of transferring photo generated electrons to surface reactions sites [27], while their MnO₂ nanostructure network structure can also be easily separated by the reactions [15], [28], [29].

To overcome the uniform interface and good dispersion highlighted in previous reports, we developed a novel photocatalyst comprising a MoSe₂/MnO₂ nanocomposite. Utilizing the hydrothermal method, we ensured the MoSe₂ component exhibited excellent

dispersibility and controllable concentrations when integrated onto the MnO₂ nanostructure. Moreover, the Fourier transform infrared (FTIR), X-ray diffraction (XRD), scanning electron microscopy (SEM), energy-dispersive X-ray spectroscopy (EDX), and high-resolution transmission electron microscopy (HR-TEM) were used to characterise the chemical properties of the obtained MoSe₂/MnO₂ nanocomposites. The adsorption performance and wide spectrum photocatalytic activity of the as-fabricated composite were investigated using the target organic contaminants Direct Yellow (DY), and the degradation of DY in solution and adsorbed on catalyst surfaces was studied under Vis and UV light irradiation, respectively. MoSe₂ and MnO₂ as single components and MoSe₂/MnO₂ as a nanocomposite were used to compare the photocatalytic efficiency.

Experimental synthesis process

2.1 Chemicals

Sodium molybdate (Na₂MoO₄) power assay 98% is purchased from the Sisco Research Laboratories Pvt. Ltd. selenium powder block (Se) assay 99%, hydrazine hydrate (N₂H₄.H₂O) assay 99%, polyvinylpyrrolidone (PVP), Manganese sulphate (MnSO₄.H₂O) assay 99%, Potassium permanganate (K₂MnO₄) assay 99.99%, Direct yellow dye (DY) (C₂₆H₁₈N₄Na₂O₈S₂), were utilized for photocatalytic Process. All chemicals were analytical grade and were applied precisely as provided. Unless otherwise noted, the experiment used laboratory-made deionised (DI) water.

2.2 Synthesis of MoSe₂

MoSe₂ were synthesised by the hydrothermal approach. In solution A, 1.20 g of Na₂MoO₄ and 0.5 g polyvinylpyrrolidone were dissolved in 50 ml of distilled water and stirred for 1 hour. Following this, in solution B, 0.8 g of selenium (Se) was added with 30 ml of N₂H₄.H₂O solution and stirred for half-an-hour separately. Subsequently, solution A is steadily added drop by drop to solution B until precipitation occurs. The resulting solution is then transferred to a 100 ml Teflon-lined autoclave and placed in an oven at 200°C for duration of 24 hours. Ultimately, the contents were subjected to centrifugation, with the resulting residue being washed using deionized water and ethanol. Following this, the residue was dried at 80°C for a period of 12 hours, yielding a pale block powder.

2.3 Synthesis of MoSe₂/MnO₂ nanocomposite

Initially, a solution comprising 50 ml of deionized water was mixed with 1.20 grams of Na₂MoO₄ and 0.8 grams of selenium (Se). After that, 2.1 grams of MnSO₄ and 1.96 grams of KMnO₄ were individually mixed with 25 ml of deionized water and prepared. Next, both the solutions were added drop by drop while continuously stirring the mixture for 1 hour. To adjust the mixture, 75 ml of deionized water was added. Subsequently, the mixture was sonicated for 30 minutes and subjected to hydrothermal treatment at 180°C for duration of 24 hours. The heterogeneous material was allowed to cool for half an hour before undergoing centrifugation. The remaining residue underwent multiple washes using ethanol and deionized water. Following the cleansing process, it was subjected to drying in a hot air oven set at 80°C for duration of 12 hours, resulting in the acquisition of MoSe₂/MnO₂ powder. The manufactured sample is detailed and subsequently employed to evaluate its photocatalytic performance. Fig.1. illustrates a schematic representation of the chemical approach utilized to produce MoSe₂/MnO₂ nanocomposites, aiding in achieving uniformity.

2.4 Photocatalysis experiment

The photocatalytic activity of a MoSe₂/MnO₂ nanocomposite was studied under direct sunlight. To begin with, 0.5 g of MoSe₂/MnO₂ nanocomposites and 20 parts per million (PPM) of coloured (DY) dye were dissolved in 100 ml of deionized distilled water (DDW) and stirred for one hour at room temperature. Following the attainment of adsorption-desorption equilibrium, the mixture was stirred in darkness for 20 minutes. Afterward, the photocatalyst suspension was subjected to UV-visible light irradiation using a 500-watt Halogen lamp [30], positioned at a 15 cm distance from the surface of the DY photocatalyst mixed solution. To ensure a consistent temperature within the photoreactor, water from the water source was re-circulated. Using a UV-Vis spectrometer (model-JASCO V-670) that measures the 200-800 nm range, 5 ml of dye mixed solution was taken from the photoreactor at certain times (every 30 minutes) for up to 120 minutes of light irradiation. The concentrations of DY in samples were determined by measuring the absorbance at 395 nm. Using the experimental synthesis technique as well as Eq. (1), we were able to find the percentage of DY degradation.

$$\text{Degradation efficiency(\%)} = \frac{(C_0 - C)}{C_0} \times 100\% \dots\dots\dots (1)$$

Where C is the concentration of DY dye at the initial stage and CO is the concentration at the final stage respectively. We used XRD and SEM analysis to study the variations in crystal structure and morphology of the composite photocatalyst after four reuse experiments.

2.5. characterizations

The X-ray diffraction analysis (Rigaku D/max ultra III diffractometer) and Cu $k\alpha$ radiation (40 K_V, $\lambda = 0.154$ nm) were used to study the crystal structure of the MoSe₂/MnO₂ nanocomposite. The XRD pattern was obtained at room temperature among the 2 theta degrees of 10° and 80°. A (JASCO V-750) instrument from Japan was used to record the UV-vis spectrum, which has a wavelength range of 200 to 800 nm. A Bruker tensor 27 Fourier transform infrared (FTIR) spectrometer model was used to look at how the nanocomposites interacted with each other. To look at the shapes, a (JEOL JSM 7500F+) SEM scanning electron microscope with an EDS detector set to 2.0 kV was used to prepare the samples. For the study, a high-resolution transmission electron microscope (HR-TEM) (JEOL JEM -2100+) working at 200 kV was used. The materials' shapes were studied based on their sizes.

3. Result and discussion

3.1. Characterization of X-Ray diffraction

Fig. 2. (a-c) shows the XRD patterns of MoSe₂, MnO₂, and MoSe₂/MnO₂, which were determined by XRD together with the samples crystallographic structures and phase compositions. For MoSe₂, there were found five strong characteristics of XRD diffraction peaks at 13.3°, 13.6°, 37.8°, 42.2° and 47.4°, which could be well assigned to (002), (100), (103), (104) and (105) diffraction planes MoSe₂ structure (JCPDS No: 01-077-1715) respectively [30]. These peaks were confirming the hexagonal structure of MoSe₂. As noted in the pattern, the MoSe₂ exhibits distinct and strong peaks, indicating a higher degree of crystallinity in the samples. In addition to these prominent peaks, supplementary low-intensity peaks within the 20° to 30° range, associated with the oxidized state of Mo, are also evident in the XRD spectra. The major diffraction peaks can be corresponding to the MnO₂ (JCPDS No: 00-044-0141), where 2θ at 6.91°, 18.1°, 28.8°, 37.5°, 41.9°, 49.8°, 60.2°, and 69.7 confirms the corresponding planes (110), (200), (310), (211), (301), (411), (521) and (541) for MnO₂ respectively [31]. The grain size (D) can be determined using the Debye–Scherrer formula, as shown in Eq. (2), which relies on the full width at half maximum (FWHM) of characteristic crystalline peaks.

$$A = \frac{K\lambda}{\beta \cos\theta}$$

where, D is the size of the particle, k is the Scherrer constant (0.9), λ is the X-ray wavelength (1.5418 Å), and β is the full width at half maximum of the particular diffraction angle (θ). The average grain sizes of the samples MnO₂, MoSe₂, and MoSe₂/MnO₂ were estimated to be 20.05 nm, 19.92 nm, and 12.46 nm respectively. The decline in the crystallite size analytically advocates that there could be the reduction in the grain roughening in the Nano composites. Moreover, the MoSe₂ lattice constant of $a = b = 3.28$ Å, $c = 12.92$ Å, MnO₂ lattice constant of $a = b = 9.78$ Å, $c = 2.86$ Å and MoSe₂/MnO₂ lattice constant of $a = b = 4.9325$ Å, $c = 6.9205$ Å respectively. In addition to these results, the lattice strain of the samples has been abbreviated to 0.0140, 0.0202, and 0.0070 respectively [32]. The XRD pattern of MoSe₂/MnO₂ clearly shows the crystalline peaks of MoSe₂ and MnO₂ which confirmed that both patterns of shows in figure.

3.2 FTIR Spectroscopy analysis

The Fourier-transform infrared (FTIR) spectra of MoSe₂ and MnO₂, recorded in the range of 400-4000 cm⁻¹, are depicted in Fig. 3. (a) and (b) respectively. The distinctive peaks detected at approximately 484 cm⁻¹, 556 cm⁻¹, 641 cm⁻¹, 781 cm⁻¹, 895 cm⁻¹, 1405 cm⁻¹ and 1405 cm⁻¹ correspond to the following chemical bonds: (Se-O-Se), (O-Mo-O), (M=O), (Se-O), (COOH), (Mo-OH), and (C-O) bonds, as well as C-H and O-H stretching vibrations, respectively [24]. MoSe₂, possessing functional groups like (-OH) and (-COOH), exhibits a negatively charged surface, rendering it highly effective for the degradation of organic dyes. The nanostructured MnO₂ displayed three vibration bands below 1000 cm⁻¹, specifically at 508 cm⁻¹, and 623 cm⁻¹. Each of these vibrational bands is characteristic of the metal-oxygen bond within the MnO₆ octahedron, whether it involves the Mn-O or Mn-O-Mn bonding, and they exhibit good consistency with previously reported results. [33]. In Fig. 3. (c), the MoSe₂/MnO₂ nanocomposite exhibits shifted peaks corresponding to (Se-O-Se), (O-Mo-O), (M=O), (Se-O), (Mo-OH) and (Mn-O), (Mn-O-Mn) bonds, which are located at 453 cm⁻¹, 609 cm⁻¹, 736 cm⁻¹, 802 cm⁻¹, 1362 cm⁻¹ and 514cm⁻¹, 611 cm⁻¹ respectively. Both XRD and FTIR analysis results provide complementary information, confirming the structural and functional characteristics of the MoSe₂/MnO₂ nanocomposite simultaneously.

3.3 UV-Vis analysis

The UV-Vis spectra of the synthesized samples are depicted in Fig. 4. (a). The absorption peaks for MoSe₂ were observed at wavelengths of 220 nm, 662 nm, 571 nm and 759 nm respectively [34]. Likewise, the absorption peaks for MnO₂ were observed at wavelengths of 214 nm, 371 nm, 447 nm and 527 nm respectively [35] whereas for the MoSe₂/MnO₂ composite, shifted peaks were observed at 218 nm, 356 nm, 436 nm, 505 nm, 647 nm, and 756 nm respectively. It is noteworthy to mention that the sample containing MoSe₂/MnO₂ exhibits the largest absorption peak, indicative of a synchronized effect between the two components. Thus, the band gap values may be inferred from the $\alpha h\nu$ versus photon energy plot (Tauc's plot) using the equation: $\alpha(h\nu)_2 = \text{const} (h\nu - E_g)^{1/2}$. The absorption coefficient, Planck's constant, the incident light frequency, and the band gap are represented by α , h , ν , and E_g , respectively [36]. Fig. 4 (b) and (c) illustrates an estimated optical band gap by using Tauc's plot relations. The calculated bandgap for MoSe₂, MnO₂ and MoSe₂/MnO₂ nanocomposite were 1.94 eV, 2.8 eV, and 4.57 eV, respectively. The observed band narrowing in the MoSe₂/MnO₂ nanocomposite indicates that the combination can effectively capture a broader spectrum of visible light, including direct sunlight. The enhanced absorption of visible light contributes to the reduction in bandgap observed in the MoSe₂/MnO₂ nanocomposite. This is believed to enhance the photocatalytic efficiency of the material when exposed to UV-visible light.

3.4 Morphology analysis

The SEM images of MoSe₂ and MoSe₂/MnO₂ were shown in Fig. 5. The prepared samples display nanoparticles that are randomly oriented and interconnected, forming a 0D network, as illustrated in Fig. 5. (a-b). The surfaces generally appear smooth, and the diameters of the nanoparticles are similar. In Fig. 5 (c-d), it is evident that the highly localized MoSe₂ nanoparticles are uniformly distributed throughout the MnO₂ nanostructure. The MoSe₂/MnO₂ nanocomposite exhibits a sheet-like structure. The photocatalytic processes of these materials stand to benefit from their large surface area, high light-collecting capacity, and efficient charge mobility [37], [38]. Furthermore, it's crucial to highlight that the shape of MoSe₂ on the nanosheet-like structures can be effectively controlled by increasing the concentrations of reactants for MoSe₂ and MoSe₂/MnO₂ composite. Additionally, the

quantity of MoSe₂ on the sheet-like structure was also enhanced during the same periods, as confirmed by the energy dispersive X-ray (EDX) spectra in Fig. 6. (a-b) and the atomic ratios provided in the table. Additionally, both MoSe₂ (Table 1) and MoSe₂/MnO₂ (Table 2) composite nanosheets were synthesized using the same hydrothermal process.

The HR-TEM images of both MoSe₂ and MoSe₂/MnO₂ nanocomposite were depicted in Fig. 7. (a-h). Notably, thin and small nanoparticle structures with MoSe₂ layers were visible in the prepared MoSe₂, as observed in the HR-TEM image captured from the sample edge. A substantial aggregation of MoSe₂, as depicted in the shaded area of the figure, suggests the successful synthesis of numerous thin MoSe₂ layers using a straightforward hydrothermal method. This observation aligns with the morphology reported in the existing literature [37]. Fig. 7. (e-h) display TEM images of MoSe₂/MnO₂ nanocomposites. As per the HR-TEM image, the prepared nanocomposite exhibited a distinct crystal structure. As anticipated, the measured d-spacing of 0.67 nm corresponds to the same value as the MoSe₂ (002) interplanar spacing [39]. Additionally, the observed d-spacing of 0.32 nm aligns with the (110) lattice of the MnO₂ nanostructure [39]. The successful formation of the MoSe₂/MnO₂ composite was confirmed by the close binding of their lattice fringes, indicating a strong interaction between the two materials. This interaction significantly enhances the electric structure at the interface, making it easier for charge carriers to separate [40]. Furthermore, the composite (002) lattice spacing of 0.70 nm for MoSe₂ was notably larger than the 0.67 nm corresponding to the (002) plane in standard MoSe₂. This discrepancy could be attributed to the replacement of Se at the Se site by O and the incorporation of O into the MoSe₂ structure.

To provide additional insight into the HR-TEM, the Energy Dispersive X-ray Spectroscopy (EDS) mapping of the composites was conducted and is depicted in Fig. 8. (a–f). The EDX spectrum reveals the presence of four elements in the composite: Mo, Se, Mn, and O. This indicates that MoSe₂ and MnO₂ in the composite were thoroughly mixed, and all four elements were uniformly distributed. The strong interaction between MoSe₂ and MnO₂ facilitated efficient movement of photocarriers, enhancing the effectiveness of the direct photocatalytic process.

3.5. X-ray photoelectron spectroscopy (XPS)

The elemental composition and binding energy of the MoSe₂/MnO₂ were analyzed using XPS, as illustrated in Fig. 9. In the XPS spectra of the MoSe₂/MnO₂ nanocomposite, peaks corresponding to the C, O, Mn, Mo, and Se elements were observed. The O 1S peak observed at 529.87 eV may be attributed to adventitious oxygen. Typically, the O 1S peak corresponds to the binding energy of oxygen atoms in a material and is often utilized as a standard for calibration purposes. The pattern of Mo 3d embedded in pure MoSe₂. It is possible to assign the peaks at 229.0 eV and 232.2 eV to the Mo 3d_{5/2} and Mo 3d_{3/2} of Mo⁴⁺, then 233.0 eV and 230.3 eV to the Mo 3d_{5/2} and Mo 3d_{3/2} of Mo⁵⁺, and 235.9 eV and 233.8 eV, to the Mo 3d_{5/2} and Mo 3d_{3/2} of Mo⁶⁺ respectively. The high-resolution Se 3d spectrum of MoSe₂, which has two peaks at 54.6 eV and 55.4 eV, respectively, correspond to both Se 3d_{5/2} and Se 3d_{3/2} of Se in MoSe₂, as previously reported [5]. To our obtained peaks of Mo 3d, Se 3d and Mn 2p core-level XPS spectra was shown in Fig. 9. (a-f) respectively. Fig. 9. (b-c) shows the Mo 3d_{5/2} and Mo 3d_{3/2} peaks of MoSe₂ which were shifted at 232.1 eV and 235.1 eV, respectively. These match up nicely with the Mo (4+) chemical states in MoSe₂. The Se 3d_{5/2} and Se 3d_{3/2} shifted peaks of MoSe₂ at 49.8 eV and 48.2 eV showed that the Se atoms were in an oxidation chemical state-2 [41]. For MnO₂ nanostructure the Mn 2p_{3/2}, Mn 2p_{1/2} and chemical state of atoms Mn⁴⁺ peaks also located at 640 eV, 652.5 eV and 642.2 eV, respectively. It also corresponds well with previously reported findings [42]. Fig. 9. (d) shows the high-resolution XPS Mn 2p spectrum of MnO₂. The shifted two peaks of Mn 2p_{3/2} (640.6 eV) and Mn 2p_{1/2} (652.5 eV), were shifted corresponding with the electronic state of Mn⁴⁺ [34]. It was confirmed by the MnO₂ presented in MoSe₂.

Notably, the peaks that correspond to Mo 3d and Se 3d, as well as the Mn 2p peaks in the composite, shifted towards lower binding energies. This shows that the MoSe₂/MnO₂ nanocomposites notably have a strong interaction [43]. Alternatively, three peaks may be seen in the O 1S spectrum. The peaks at 529.8 eV, 531.0 eV, and 532.4 eV in Fig. 9 (e) were identified as the lattice oxygen (Mn-O-Mn) surface absorption hydroxyl groups (Mn-OH) and the water that was absorbed on the surface of the material [44]. The Deconvoluting the C 1S signals into three Gaussian peaks allows for the detection of different chemical states of carbon atoms, as shown in Fig. 9 (f). The strong peak 2 at 284.4 eV is the binding energy of C atoms in the carbon structure with C-C. The small peaks at 285.9 eV and 288.5 eV are the binding energies of carbon from the C-O bond and the C=O-C bond, respectively [45]. In the combination, the hydroxyl group's peak moved slightly towards higher binding energy. In

this case, it suggests that the electron density of the surface hydroxyl groups decreased in the MoSe₂/MnO₂ nanocomposite. This phenomenon could be attributed to the strong interfacial interactions present in the MoSe₂/MnO₂ nanocomposite. It is also interesting that the greatly higher hydroxyl content on the composite's surface might not only enhance contaminant adsorption via hydrogen production, but also function as electron donors for photogenerated holes (h⁺). These holes might then be further oxidised to OH⁻, which allows improved separating of photogenerated carriers and enhancing photocatalytic process.

3.6. Light absorption and photocatalytic properties

To evaluate the photocatalytic performance of the photocatalyst, we employed an organic dye (Direct Yellow) as a model pollutant and the photodegradation occurred under UV-Vis light irradiation. Fig. 10. (a-f) shows the UV-Vis absorbance spectrum of DY dye degrading over (a) MoSe₂, (b) MnO₂, and (c) MoSe₂/MnO₂ at 120 minutes. The absorption of dye solution doesn't change the optimal conditions for absorption and release in large quantities Fig. 10 (d) displays the photo standard behaviour of the DY dye as analysed in a black test experiment with the photocatalyst adsorption. The MoSe₂, MnO₂ and MoSe₂/MnO₂ nanocomposite are added to the DY dye solution, and the solution is investigated for 120 min. In comparison to MoSe₂, the MoSe₂/MnO₂ nanocomposite demonstrates enhanced catalytic performance for the degradation of DY dye when exposed to under UV-Vis light.

The kinetics of the photocatalytic degradation of DY dye were assessed using Equation (2),

$$\ln \frac{C_t}{C_0} = -kt \dots\dots\dots (2)$$

Where, C₀ is the initial concentration of the DY dye and C_t is the final concentration at the time; k is the pseudo first-order rate constant (min⁻¹). The pseudo-first order kinetics plot is shown in Fig. 10. (e) are shown in table 1: (1) The dye concentration in ppm, (2) degradation efficiency in percentage, (3) kinetic equation, (4) rate constant in k, (5) time in minutes, and (6) R² values of MoSe₂, MnO₂, and MoSe₂/MnO₂ nanocomposite. From table. 3. The rate constant of MoSe₂ was 0.0290 min⁻¹, the highest among others 0.0136 min⁻¹ for MnO₂ and 0.1294 min⁻¹ for MoSe₂/MnO₂. The enhanced photocatalytic activity observed for MoSe₂/MnO₂ was attributed to its morphology. As photocatalysis is a surface phenomenon, therefore the activation of a large surface area is in proportion larger than the quantity of reactive oxygen species produced. The MnO₂ catalyst improves the interaction with DY molecules and dissolves in DI water. Consequently, MoSe₂/MnO₂ exhibited higher

photocatalytic efficiency compared to MoSe₂ alone. Therefore, the photocatalytic efficiency of MoSe₂/MnO₂ was superior to that of MoSe₂. Fig. 10 (f) shows the degradation efficiency of the produced photocatalysis under UV-Vis light irradiation. In the as-made materials, the photocatalytic degradation efficiency reached 96% for MoSe₂/MnO₂. Further investigation revealed that the MoSe₂/MnO₂ composite maintained excellent adsorption and photocatalytic activity. While the adsorption and photocatalytic synergistic reduction rate of Direct Yellow (DY) may have been somewhat lower, the MoSe₂/MnO₂ composite still exhibited enhanced adsorption and photocatalytic activity, along with improved durability.

Table 3

1) The Dye concentration in ppm, 2) Efficiency of degradation (%), (3) Kinetic equation, (4) Rate constant (k), (5) time (min) and (6) R² values are listed.

3.7. Photocatalytic mechanism of MoSe₂/MnO₂ Nanocomposite

Fig.11. illustrates a potential photocatalytic mechanism under irradiation. The observed changes in photocatalytic activity are attributed to variations in phase growth and morphological alterations associated with reduction and oxidation processes. The photocatalytic mechanism typically involves three main steps: (i) Absorption of photons with energy greater than the bandgap of the photocatalyst; (ii) separation, migration, or recombination of electron-hole pairs; and (iii) redox reactions occurring at the surface of the photocatalyst. In general, surface imperfections can serve as sites for the absorption of oxygen and water. Semiconductor photocatalysts, when exposed to air or oxygen, can effectively degrade numerous organic pollutants. When activated by UV-Vis light (hν), MoSe₂/MnO₂ generates electron-hole pairs, which act as strong antioxidants and reducing agents. The photocatalyst exhibits efficient performance because holes and photovoltaic electrons do not readily recombine on the surface of the semiconductor. The following expressions outline the photocatalytic mechanisms for the degradation of DY dyes (3)-(9). To enhance photocatalytic activity, the electrons that are produced by light engage in an oxidation-reduction process before recombination. The production of the electron-hole pairs in MoSe₂/MnO₂ nanocomposite in the absence of UV-Vis light is an accelerated oxidation process in which electrons are activated from VB via substantial light absorption Eq (3). However, when oxygen molecules are absorbed by the excited electrons (ecb-), a number of

reactive substances are formed, including superoxide ($\bullet\text{O}_2^-$), hydroxyl ($\bullet\text{OH}$) radicals, and hydrogen peroxide (H_2O_2) Eq. (4-6) [19]

The formation of highly oxidizable positively charged holes (hVB^+) under visible light, on the other together, indicates that their source might instantly carry out the oxidative degradation of a yellow dye. In addition, another component of the holes known as hVB^+ reacts with the absorbed H_2O and OH^- in the DY solution to generate hydroxyl ($\bullet\text{OH}$) radicals (Eq. 7 and 8) [19] as a result. A powerful oxidant, hydroxyl radicals ($\bullet\text{OH}$) may be converted into water and carbon dioxide, two substances that are good for the environment. Eq. (9). $\text{MoSe}_2/\text{MnO}_2$ induces of $\bullet\text{OH}$ radicals and contributes to the development of the dye degradation process. The shortage of super oxide emit can also be seen in the measurements. So, this means that hydroxyl radicals make it possible for the dye degradation. Overall, it was determined that the synthetic $\text{MoSe}_2/\text{MnO}_2$ composite that has been created showed strong photocatalytic activity when it is exposed to UV light. As a result of influence of the synthesised sample size, quantum confinement, and the catalyst, the energy band gap as the thickness increases gradually towards it crosses the nanoscale. Additionally, the generated photocatalysts' performance in degrading organic pollutants was similar to that of the prior study and is shown in Table 4. In Fig. 11. the proposed photocatalytic mechanism of $\text{MoSe}_2/\text{MnO}_2$ for the degradation of DY dye is depicted schematically.

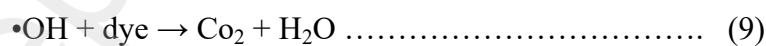
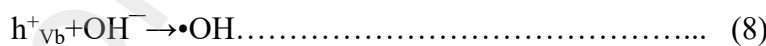
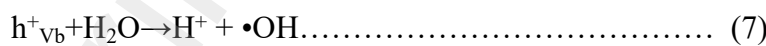
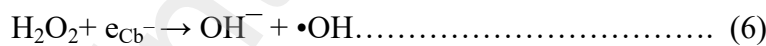


Table 4

Comparison of our present work and earlier work.

4. Conclusion

We have successfully developed and synthesized a MoSe₂/MnO₂ nanocomposite with enhanced photocatalytic performance using a simple hydrothermal approach. The interface contact, surface morphology, and loading quantities of MoSe₂ can be precisely controlled by adjusting the reaction conditions. Under UV-Vis light irradiation, MoSe₂ exhibited a maximum absorption-photocatalytic removal rate of 55%, while MnO₂ demonstrated 47%. However, the MoSe₂/MnO₂ composite surpassed both individual components with a remarkable removal rate of 96% for Direct Yellow (DY) within 120 minutes. Moreover, the MoSe₂/MnO₂ nanocomposite exhibited excellent separation efficiency, retained stable shape, and maintained structural stability, all of which are advantageous for cyclic photocatalytic removal of water pollutants. Our study provides a fundamental understanding of the charge generation, separation, and transfer processes occurring in the MoSe₂/MnO₂ nanocomposite under UV-Vis light. The enhanced photocatalytic activity can be attributed to efficient wide-spectrum absorption, a large surface area, rapid electron transfer, and stable and uniform interface contacts. The concepts, techniques, and results obtained in this study could be valuable for the development of prospective photocatalysts with the capability for reducing H₂O and CO₂ under UV-Vis light. Our investigation thoroughly examined the photocatalytic performance of these nanostructures under both ultraviolet UV-Vis light. Our findings unequivocally demonstrate that the MoSe₂/MnO₂ nanocomposite exhibits exceptional responsiveness to UV-Vis light and delivers outstanding photocatalytic efficiency.

Data availability Data

Data will be made available on request.

Preprint not peer reviewed

References:

- [1] Y. Qu und X. Duan, “Progress, challenge and perspective of heterogeneous photocatalysts”, *Chem Soc Rev*, Bd. 42, Nr. 7, S. 2568–2580, März 2013, doi: 10.1039/c2cs35355e.
- [2] P. Zhou, J. Yu, und M. Jaroniec, “All-solid-state Z-scheme photocatalytic systems”, *Advanced Materials*, Bd. 26, Nr. 29. Wiley-VCH Verlag, S. 4920–4935, 6. August 2014. doi: 10.1002/adma.201400288.
- [3] H. Wang u. a., “Semiconductor heterojunction photocatalysts: Design, construction, and photocatalytic performances”, *Chemical Society Reviews*, Bd. 43, Nr. 15. Royal Society of Chemistry, S. 5234–5244, 7. August 2014. doi: 10.1039/c4cs00126e.
- [4] Y. Li, Q. Wang, H. Wang, J. Tian, und H. Cui, “Novel Ag₂O nanoparticles modified MoS₂ nanoflowers for piezoelectric-assisted full solar spectrum photocatalysis”, 2018.
- [5] H. Chu u. a., “Hexagonal 2H-MoSe₂ broad spectrum active photocatalyst for Cr (VI) reduction”, *Sci Rep*, Bd. 6, Okt. 2016, doi: 10.1038/srep35304.
- [6] R. J. Tayade, P. K. Surolia, R. G. Kulkarni, und R. V. Jasra, “Photocatalytic degradation of dyes and organic contaminants in water using nanocrystalline anatase and rutile TiO₂”, *Sci Technol Adv Mater*, Bd. 8, Nr. 6, S. 455–462, Sep. 2007, doi: 10.1016/j.stam.2007.05.006.
- [7] S. Singh, R. Pendurthi, M. Khanuja, S. S. Islam, S. Rajput, und S. M. Shivaprasad, “Copper-doped modified ZnO nanorods to tailor its light assisted charge transfer reactions exploited for photo-electrochemical and photo-catalytic application in environmental remediation”, *Appl Phys A Mater Sci Process*, Bd. 123, Nr. 3, März 2017, doi: 10.1007/s00339-017-0806-8.
- [8] R. Sharma, Uma, S. Singh, A. Verma, und M. Khanuja, “Visible light induced bactericidal and photocatalytic activity of hydrothermally synthesized BiVO₄ nano-octahedrals”, *J Photochem Photobiol B*, Bd. 162, S. 266–272, Sep. 2016, doi: 10.1016/j.jphotobiol.2016.06.035.
- [9] S. Yang u. a., “Molybdenum diselenide nanosheet/carbon nanofiber heterojunctions: Controllable fabrication and enhanced photocatalytic properties with a broad-spectrum

- response from visible to infrared light”, *J Colloid Interface Sci*, Bd. 518, S. 1–10, Mai 2018, doi: 10.1016/j.jcis.2018.01.099.
- [10] H. Jiang, “Electronic band structures of molybdenum and tungsten dichalcogenides by the GW approach”, *Journal of Physical Chemistry C*, Bd. 116, Nr. 14, S. 7664–7671, Apr. 2012, doi: 10.1021/jp300079d.
- [11] R. Coehoorn, C. Haas, J. Dijkstra, C. J. F. Flipse, R. A. De Groot, und A. Wold, “Electronic structure of MoSe₂, MoS₂, and WSe₂. I. Band-structure calculations and photoelectron spectroscopy”.
- [12] D. Zeng u. a., “Construction of network-like and flower-like 2H-MoSe₂ nanostructures coupled with porous g-C₃N₄ for noble-metal-free photocatalytic H₂ evolution under visible light”, *Appl Catalyt B*, Bd. 233, S. 26–34, Okt. 2018, doi: 10.1016/j.apcatb.2018.03.102.
- [13] Y. Wang u. a., “Construction of Z-scheme MoSe₂/CdSe hollow nanostructure with enhanced full spectrum photocatalytic activity”, *Appl Catal B*, Bd. 244, S. 76–86, Mai 2019, doi: 10.1016/j.apcatb.2018.11.033.
- [14] T. Xie, Y. Liu, H. Wang, und Z. Wu, “Layered MoSe₂ /Bi₂WO₆ composite with P-N heterojunctions as a promising visible-light induced photocatalyst”, *Appl Surf Sci*, Bd. 444, S. 320–329, Juni 2018, doi: 10.1016/j.apsusc.2018.03.072.
- [15] I. Khan, M. Sadiq, I. Khan, und K. Saeed, “Manganese dioxide nanoparticles/activated carbon composite as efficient UV and visible-light photocatalyst”, *Environmental Science and Pollution Research*, Bd. 26, Nr. 5, S. 5140–5154, Feb. 2019, doi: 10.1007/s11356-018-4055-y.
- [16] Y. Shi u. a., “2D/1D protonated g-C₃N₄/α-MnO₂ Z-scheme heterojunction with enhanced visible-light photocatalytic efficiency”, *Ceram Int*, Bd. 46, Nr. 16, S. 25905–25914, Nov. 2020, doi: 10.1016/j.ceramint.2020.07.075.
- [17] S. Panimalar u. a., “Studies of MnO₂/g-C₃N₄ heterostructure efficient of visible light photocatalyst for pollutants degradation by sol-gel technique”, *Surfaces and Interfaces*, Bd. 20, Sep. 2020, doi: 10.1016/j.surfin.2020.100512.
- [18] J. Zhao, J. Nan, Z. Zhao, N. Li, J. Liu, und F. Cui, “Energy-efficient fabrication of a novel multivalence Mn₃O₄-MnO₂ heterojunction for dye degradation under visible

- light irradiation”, *Appl Catal B*, Bd. 202, S. 509–517, März 2017, doi: 10.1016/j.apcatb.2016.09.065.
- [19] H. Mittal und M. Khanuja, “Nanosheets-and nano-urchins-like nanostructures of MoSe₂ for photocatalytic water purification: kinetics and reusability study”, doi: 10.1007/s11356-019-06275-8/Published.
- [20] H. Xu, J. Zhang, Y. Chen, H. Lu, J. Zhuang, und J. Li, “Synthesis of polyaniline-modified MnO₂ composite nanorods and their photocatalytic application”, *Mater Lett*, Bd. 117, S. 21–23, Feb. 2014, doi: 10.1016/j.matlet.2013.11.089.
- [21] B. Yin, S. Zhang, Y. Jiao, Y. Liu, F. Qu, und X. Wu, “Crystl Eng Comm Facile synthesis of ultralong MnO₂ nanowires as high-performance supercapacitor electrodes and photocatalysts with enhanced photocatalytic activities”. [Online]. Verfügbar unter: www.rsc.org/crystengcomm
- [22] X. Zheng, L. Yang, Y. Li, L. Yang, und S. Luo, “Direct Z-scheme MoSe₂ decorating TiO₂ nanotube arrays photocatalyst for water decontamination”, *Electrochim Acta*, Bd. 298, S. 663–669, März 2019, doi: 10.1016/j.electacta.2018.12.130.
- [23] J. Zhang, X. Zan, X. Shen, und H. Zheng, “Preparation of direct Z-scheme hierarchical MoS₂/MnO₂ composite for efficient adsorption and wide spectrum photocatalytic degradation of organic pollutants in water”. [Online]. Verfügbar unter: <https://ssrn.com/abstract=4279267>
- [24] I. Siddiqui, H. Mittal, V. K. Kohli, P. Gautam, M. Ali, und M. Khanuja, “Hydrothermally synthesized micron sized, broom-shaped MoSe₂ nanostructures for superior photocatalytic water purification”, *Mater Res Express*, Bd. 5, Nr. 12, Dez. 2018, doi: 10.1088/2053-1591/aae241.
- [25] M. Xue u. a., “The direct synthesis of mesoporous structured MnO₂/TiO₂ nanocomposite: A novel visible-light active photocatalyst with large pore size”, *Nanotechnology*, Bd. 19, Nr. 18, Mai 2008, doi: 10.1088/0957-4484/19/18/185604.
- [26] X. Zheng, Z. Han, W. Yang, F. Qu, B. Liu, und X. Wu, “3D Co₃O₄@MnO₂ heterostructures grown on a flexible substrate and their applications in supercapacitor electrodes and photocatalysts”, *Dalton Transactions*, Bd. 45, Nr. 42, S. 16850–16858, 2016, doi: 10.1039/c6dt03076a.

- [27] J. Fei u. a., “Controlled preparation of MnO₂ hierarchical hollow nanostructures and their application in water treatment”, *Advanced Materials*, Bd. 20, Nr. 3, S. 452–456, Feb. 2008, doi: 10.1002/adma.200701231.
- [28] M. F. Warsi, M. Bilal, S. Zulfiqar, M. U. Khalid, P. O. Agboola, und I. Shakir, “Enhanced visible light driven Photocatalytic activity of MnO₂ nanomaterials and their hybrid structure with carbon nanotubes”, *Mater Res Express*, Bd. 7, Nr. 10, Okt. 2020, doi: 10.1088/2053-1591/abbf8d.
- [29] M. Sugantha, P. A. Ramakrishnan, A. M. Hermann, C. P. Warmsingh, und D. S. Ginley, “Nanostructured MnO₂ for Li batteries”, 2003. [Online]. Verfügbar unter: www.sciencedirect.com/elsevier.com/locate/ijhydene
- [30] J. Sawadogo, M. Bougouma, J. Legma, und M. Ogletree, “Determination of stoichiometry from polycrystalline powders of transition metals lamellar dichalcogenides: MoSe₂, WSe₂, obtained by synthesis in laboratory”, *Int J Biol Chem Sci*, Bd. 9, Nr. 1, S. 454, Juni 2015, doi: 10.4314/ijbcs.v9i1.39.
- [31] C. Shi u. a., “Synthesis of layered MnO₂ nanosheets for enhanced oxygen reduction reaction catalytic activity”, *Electrochim Acta*, Bd. 132, S. 239–243, Juni 2014, doi: 10.1016/j.electacta.2014.03.150.
- [32] T. Elangovan, P. Kuppasami, R. Thirumurugesan, C. Sudha, E. Mohandas, und D. Mangalaraj, “A study on the influence of copper content in CrN/Cu nanocomposite thin films prepared by pulsed dc magnetron sputtering”, in *Journal of Nanoscience and Nanotechnology*, Sep. 2009, S. 5436–5440. doi: 10.1166/jnn.2009.1129.
- [33] M. F. Warsi, M. Bilal, S. Zulfiqar, M. U. Khalid, P. O. Agboola, und I. Shakir, “Enhanced visible light driven Photocatalytic activity of MnO₂ nanomaterials and their hybrid structure with carbon nanotubes”, *Mater Res Express*, Bd. 7, Nr. 10, Okt. 2020, doi: 10.1088/2053-1591/abbf8d.
- [34] H. Mittal, A. Ivaturi, und M. Khanuja, “MoSe₂-modified ZIF-8 novel nanocomposite for photocatalytic remediation of textile dye and antibiotic-contaminated wastewater”, *Environmental Science and Pollution Research*, Bd. 30, Nr. 2, S. 4151–4165, Jan. 2023, doi: 10.1007/s11356-022-22487-x.

- [35] S. Vijayalakshmi und E. Kumar, "Synthesis and Investigations on structural, optical, thermal and electrical conductivity of α -MnO₂ nanoparticles", 2019. [Online]. Verfügbar unter: <https://www.researchgate.net/publication/335397323>
- [36] S. M. EL-Dafrawy, M. Tarek, S. Samra, und S. M. Hassan, "Synthesis, photocatalytic and antidiabetic properties of ZnO/PVA nanoparticles", *Sci Rep*, Bd. 11, Nr. 1, Dez. 2021, doi: 10.1038/s41598-021-90846-8.
- [37] Z. Lu u. a., "Enhanced interfacial electron transfer and boosted visible-light photocatalytic hydrogen evolution activity of g-C₃N₄ by noble-metal-free MoSe₂ nanoparticles", *J Mater Sci*, Bd. 55, Nr. 27, S. 13114–13126, Sep. 2020, doi: 10.1007/s10853-020-04945-4.
- [38] M. F. Warsi, M. Bilal, S. Zulfiqar, M. U. Khalid, P. O. Agboola, und I. Shakir, "Enhanced visible light driven Photocatalytic activity of MnO₂ nanomaterials and their hybrid structure with carbon nanotubes", *Mater Res Express*, Bd. 7, Nr. 10, Okt. 2020, doi: 10.1088/2053-1591/abbf8d.
- [39] S. Rong, T. He, und P. Zhang, "Self-assembly of MnO₂ nanostructures into high purity three-dimensional framework for high efficiency formaldehyde mineralization", *Appl Catal B*, Bd. 267, Juni 2020, doi: 10.1016/j.apcatb.2019.118375.
- [40] J. Zhang, Y. Hu, H. Zheng, und P. Zhang, "Hierarchical Z-scheme 1D/2D architecture with TiO₂ nanowires decorated by MnO₂ nanosheets for efficient adsorption and full spectrum photocatalytic degradation of organic pollutants", *Catal Sci Technol*, Bd. 10, Nr. 11, S. 3603–3612, Juni 2020, doi: 10.1039/d0cy00419g.
- [41] J. Lu u. a., "Identifying and Visualizing the Edge Terminations of Single-Layer MoSe₂ Island Epitaxially Grown on Au (111)", *ACS Nano*, Bd. 11, Nr. 2, S. 1689–1695, Feb. 2017, doi: 10.1021/acsnano.6b07512.
- [42] A. E. Reddy u. a., "Fabrication of a snail shell-like structured MnO₂@CoNiO₂ composite electrode for high performance supercapacitors", *RSC Adv*, Bd. 7, Nr. 20, S. 12301–12308, 2017, doi: 10.1039/c7ra01126a.
- [43] X. Li und K. Peng, "MoSe₂/montmorillonite composite nanosheets: Hydrothermal synthesis, structural characteristics, and enhanced photocatalytic activity", *Minerals*, Bd. 8, Nr. 7, Juli 2018, doi: 10.3390/min8070268.

- [44] Z. Li, W. Kang, Z. Han, J. Yan, B. Cheng, and Y. Liu, "Hierarchical MnOx@PVDF/MWCNTs tree-like nanofiber membrane with high catalytic oxidation activity", *J Alloys Compd*, Bd. 780, S. 805–815, Apr. 2019, doi: 10.1016/j.jallcom.2018.11.405.
- [45] L. Huang, X. Luo, C. Chen, and Q. Jiang, "A high specific capacity aqueous zinc-manganese battery with a ϵ -MnO₂ cathode", *Ionics (Kiel)*, Bd. 27, Nr. 9, S. 3933–3941, Sep. 2021, doi: 10.1007/s11581-021-04160-4.
- [46] D. Monga und S. Basu, "Tuning the photocatalytic/electrocatalytic properties of MoS₂/MoSe₂ heterostructures by varying the weight ratios for enhanced wastewater treatment and hydrogen production", *RSC Adv*, Bd. 11, Nr. 37, S. 22585–22597, Juni 2021, doi: 10.1039/d1ra01760h.
- [47] G. Khabiri u. a., "A novel α -Fe₂O₃@MoS₂QDs heterostructure for enhanced visible-light photocatalytic performance using ultrasonication approach", *Ceram Int*, Bd. 46, Nr. 11, S. 19600–19608, Aug. 2020, doi: 10.1016/j.ceramint.2020.05.021.
- [48] J. Zhang, X. Zan, X. Shen, and H. Zheng, "Preparation of direct Z-scheme hierarchical MoS₂/MnO₂ composite for efficient adsorption and wide spectrum photocatalytic degradation of organic pollutants in water". [Online]. Verfügbar unter: <https://ssrn.com/abstract=4279267>
- [49] I. Siddiqui, H. Mittal, V. K. Kohli, P. Gautam, M. Ali, und M. Khanuja, "Hydrothermally synthesized micron sized, broom-shaped MoSe₂ nanostructures for superior photocatalytic water purification", *Mater Res Express*, Bd. 5, Nr. 12, Dez. 2018, doi: 10.1088/2053-1591/aae241.
- [50] J. Zhao, J. Nan, Z. Zhao, N. Li, J. Liu, und F. Cui, "Energy-efficient fabrication of a novel multivalence Mn₃O₄-MnO₂ heterojunction for dye degradation under visible light irradiation", *Appl Catal B*, Bd. 202, S. 509–517, März 2017, doi: 10.1016/j.apcatb.2016.09.065.
- [51] X. Zheng, Z. Han, W. Yang, F. Qu, B. Liu, und X. Wu, "3D Co₃O₄@MnO₂ heterostructures grown on a flexible substrate and their applications in supercapacitor electrodes and photocatalysts", *Dalton Transactions*, Bd. 45, Nr. 42, S. 16850–16858, 2016, doi: 10.1039/c6dt03076a.

Preprint not peer reviewed